

Boise State University ScholarWorks

Mechanical and Biomedical Engineering Faculty
Publications and Presentations

Department of Mechanical and Biomedical
Engineering

8-1-2017

Dynamic Rating of Overhead Transmission Lines over Complex Terrain Using a Large-Eddy Simulation Paradigm

Tyler Phillips
Boise State University

Ray DeLeon
Boise State University

Inanc Senocak
Boise State University

Publication Information

Phillips, Tyler; DeLeon, Ray; and Senocak, Inanc. (2017). "Dynamic Rating of Overhead Transmission Lines over Complex Terrain Using a Large-Eddy Simulation Paradigm". *Renewable Energy*, 108, 380-389. <https://doi.org/10.1016/j.renene.2017.02.072>



This is an author-produced, peer-reviewed version of this article. © 2017, Elsevier. Licensed under the Creative Commons Attribution-Non Commercial-No Derivatives 4.0 license. <http://creativecommons.org/licenses/by-nc-nd/4.0/>. The final, definitive version of this document can be found online at *Renewable Energy*, doi: [10.1016/j.renene.2017.02.072](https://doi.org/10.1016/j.renene.2017.02.072)

1 Dynamic rating of overhead transmission lines over
2 complex terrain using a large-eddy simulation paradigm

3 Tyler Phillips^a, Rey DeLeon^{a,b}, Inanc Senocak^{a,*}

4 ^a*Department of Mechanical & Biomedical Engineering*
5 *Boise State University, Boise, Idaho 83725*

6 ^b*Department of Mechanical Engineering*
7 *University of Idaho, Moscow, Idaho 83844*

8 **Abstract**

9 Dynamic Line Rating (DLR) enables rating of power line conductors using real-
10 time weather conditions. Conductors are typically operated based on a con-
11 servative static rating that assumes worst case weather conditions to avoid line
12 sagging to unsafe levels. Static ratings can cause unnecessary congestion on
13 transmission lines. To address this potential issue, a simulation-based dynamic
14 line rating approach is applied to an area with moderately complex terrain.
15 A micro-scale wind solver — accelerated on multiple graphics processing units
16 (GPUs) — is deployed to compute wind speed and direction in the vicinity of
17 powerlines. The wind solver adopts the large-eddy simulation technique and
18 the immersed boundary method with fine spatial resolutions to improve the
19 accuracy of wind field predictions. Statistical analysis of simulated winds com-
20 pare favorably against wind data collected at multiple weather stations across
21 the testbed area. The simulation data is then used to compute excess trans-
22 mission capacity that may not be utilized because of a static rating practice.
23 Our results show that the present multi-GPU accelerated simulation-based ap-
24 proach — supported with transient calculation of conductor temperature with
25 high-order schemes — could be used as a non-intrusive smart-grid technology
26 to increase transmission capacity on existing lines.

27 *Keywords:*

28 Computational Fluid Dynamics, Dynamic Line Rating, Wind Power

*Corresponding author. Tel.: +1 208 426 4066. E-mail: senocak@boisestate.edu
Preprint submitted to Renewable Energy *February 20, 2017*

29 **1. Introduction**

30 Investments in renewable energy has been driven by several factors, including
31 energy security and stability, climate change, and economics. Since 2000, wind
32 energy has been the largest source of new renewable generation installed in the
33 United States [1]. However, wind power generation is much more complex than
34 installing wind turbines in windy areas. Grid integration is a major challenge,
35 many of the best locations for wind farms do not have access to the needed
36 transmission capacity [2]. Congestion in existing transmission lines is a growing
37 concern, resulting in inefficiencies for both renewable energy producers, utilities
38 and balancing authorities [3]. At times, transmission service providers (TSPs)
39 may not be able to absorb the power generated, therefore, power production
40 can be curtailed.

41 Potential sites for wind power generation are usually found in remote open
42 areas that are away from populated cities, where electricity is needed most.
43 Historically, transmission systems have been built together with power produc-
44 tion installations in order to meet the electricity demand. For economic reasons
45 they are usually not over-sized, therefore, current transmission networks in many
46 of these sites may not support additional generation. Many wind projects have
47 been able to patch into the existing transmission network, however, these oppor-
48 tunities are shrinking. Further expansion of wind energy may require large in-
49 vestments in transmission networks, creating an obstacle for cost-effective wind
50 deployment [1, 4].

51 Transmission capacity can be increased in several ways. The obvious way
52 is to reinforce the transmission network with new powerlines. However, this
53 is constrained by the high costs and legal challenges of building new power-
54 lines [5]. Therefore, TSPs have focused on innovative solutions that modifies
55 existing network to increase transmission capacity. Different techniques include
56 prediction of meteorological conditions by means of deterministic [6] or proba-
57 bilistic [7] forecasting methods, and adopting the newest innovations in smart-
58 grid real-time monitoring of temperature, sag, tilt, power, current and weather

59 conditions [8, 9, 10]. In the case of wind energy integration, monitoring meteo-
60 rological conditions in real-time can be very beneficial for both power generation
61 and transmission purposes. Strong winds needed for wind generation, will also
62 cool down the conductor of local transmission lines, creating additional capacity,
63 which would enable TSPs to “overload” the line when it is needed most [11, 12].

64 Transmission conductor capacity is limited by its maximum allowable tem-
65 perature. The maximum amount of electric current a conductor can transmit
66 before structural damage is known as *ampacity*. Currently, ampacity is gen-
67 erally determined using a static line rating (SLR) methodology. SLR is based
68 on conservative assumptions regarding environmental conditions, such as high
69 ambient temperature and low wind conditions. These assumptions were made
70 to avoid lines sagging to unsafe levels. However, they are overly conservative
71 for areas where wind generation is abundant. Therefore, TSPs are investigating
72 dynamic line rating (DLR) methods to increase ampacity on existing lines. DLR
73 utilizes real-time environmental conditions to better predict the temperature of
74 the conductor. Deployment of DLR has the potential to reduce the estimated
75 \$60 billion needed in transmission infrastructure to meet the 20% wind energy
76 by 2030 [2].

77 Fernandez et al. [13] provide a comprehensive review of real-time DLR
78 technologies that have been developed over the last 30 years, endorsing the
79 potential of DLR for wind power integration. Commercially available DLR
80 technologies include direct line sag, line tension, and conductor temperature
81 measurements [14]. Wind turbines are increasingly being built in areas of com-
82 plex terrain, as available sites on flat terrain is diminishing. In complex terrain
83 elevated positions like hill tops are favorable sites due to the increased wind
84 speed. However, complex terrain proves to be challenging for the aforemen-
85 tioned DLR systems. Sag and tension monitoring systems can only inform
86 TSPs of the average sag or tension measurement over large sectionalized trans-
87 mission spans, therefore, only the average temperature of the conductor over
88 large sections can be known. Direct temperature measurements at a single lo-
89 cation may not necessarily represent the critical span, or the hottest section

90 along a conductor. Studies have shown that conductor temperature can vary
91 spatially by 10–20°C due to variations in wind speed and direction [15, 16, 17].
92 Therefore, currently adopted DLR systems may not be a good solution for de-
93 termining the real-time transmission capacity in regions of complex terrain. If
94 implemented, they may potentially lead to severe overestimation of the actual
95 ratings, allowing the conductor to be overloaded and causing degradation of the
96 line. Adding more monitoring devices could be a solution, however these sys-
97 tems are typically expensive for wide deployment that is needed to reduce risks
98 to an acceptable level [18]. Additionally, implementation of direct DLR systems
99 can prove to be challenging, as transmission lines need to be de-energized during
100 installation and regular maintenance. Therefore, a non-intrusive DLR solution
101 is highly desirable, which also motivates the present study.

102 In Greenwood et al. [19] two non-intrusive approaches were compared. One
103 approach adopted a CFD-based library approach to extract wind speeds and
104 direction along the path of transmission lines and the other approach used an
105 uncertainty model based on a small number of weather stations. Greenwood
106 et al. suggested that a more sophisticated wind model that can accurately
107 capture the time-dependent nature of winds over complex terrain coupled with
108 uncertainty quantification would be invaluable to expand the DLR concept.
109 Michiorri et al. [20] used actual environmental conditions from a limited number
110 of meteorological stations as input to the steady-state thermal models. An
111 inverse distance interpolation technique and a power law for wind profile were
112 used to estimate the environmental conditions at transmission line. A state-
113 estimation algorithm based on the Monte-Carlo approach was then used to take
114 into account the uncertainty in data. Michiorri et al identified the source of
115 errors as the physical models used in their approach, and suggested the use of
116 wind flow models based on the computational fluid dynamics (CFD) approach.

117 With today’s improved wind and weather modeling and high performance
118 computing capabilities, the use of computer simulations to forecast wind and
119 determine transmission capacity has emerged as an alternative to intrusive hard-
120 ware solutions. Short-term wind forecasting can potentially be a valuable tool

121 for TSPs, enabling conductor temperature calculations at dense intervals along
122 transmission lines in complex terrain. Michiorri et al. [21] reviewed current me-
123 teorological forecasting technologies for broadening the adoption of DLR and
124 particularly drew attention to the current need to improve low wind speed mod-
125 eling and turbulence. Michiorri et al. promote the viewpoint of moving from
126 monitoring technologies to an active management technology where wind fore-
127 casting for different time horizons becomes critical. To this end, our large-eddy
128 simulation approach directly addresses the need to improve low wind speed
129 modeling in the vicinity of transmission lines.

130 Meso-scale numerical weather prediction models have long been used to
131 forecast winds and other meteorological variables, however their application to
132 micro-scale atmospheric boundary layer flows over complex terrain with a hor-
133 izontal spatial resolution ranging from 10 to 100m is still an on-going research
134 and far from realizing the forecasting mode. Mesoscale weather forecasting
135 models typically adopt spatial resolutions on the order of a few kilometers. Re-
136 sults from existing forecasting models vary greatly depending on the locations and
137 time period investigated [22, 23, 24, 25, 26]. On relatively flat terrain use of
138 mesoscale models may prove effective, but fine-scale forecasting solutions that
139 can resolve complex terrain features with horizontal resolution on the order of
140 10m are needed. For instance micro-scale complex terrain forecasting models
141 could be used to quantify the stochastic variations in line ratings, which could
142 then be converted to dynamic constraints as described by Banerjee et al. [27].

143 In what follows, we present the equations for dynamic line rating, followed
144 by our massively parallel micro-scale wind solver to predict wind speed and
145 direction as a function of time. An actual test area with moderately complex
146 terrain is simulated, and predictions are compared against available weather
147 station data at multiple locations. Field and simulation data are then used to
148 compute available ampacity for a dynamic line rating scenario, demonstrating
149 the potential of the current non-intrusive approach to increase transmission
150 capacity.

151 2. IEEE Standard 738-2012 transmission capacity calculation

152 Transmission line capacity is commonly calculated using procedures de-
153 scribed either in the Institute of Electrical and Electronics Engineers (IEEE)
154 738 Standard [28] or the CIGRE Standard [29]. In this study, we follow the
155 IEEE standard and describe the salient features of the calculation procedure for
156 clarity.

157 Temperature of an overhead electrical conductor is a function of its material
158 properties, weather conditions, and electrical current. The steady-state heat
159 balance is given as

$$160 \quad q_c + q_r = q_s + q_j, \quad (1)$$

161 where q_c , q_r , q_s , and q_j are the conductor convective heat loss, radiated heat
162 loss, solar heat gain, and Joule heating, respectively.

163 Joule heating is calculated using the electric current, I , and conductor re-
164 sistance, $R(T_{ave})$, which is a function of its average temperature, T_{ave} . Joule
165 heating is given as

$$166 \quad q_j = I^2 \cdot R(T_{ave}). \quad (2)$$

167 The steady-state thermal rating used to calculate conductor capacity is then
168 expressed as

$$169 \quad I = \sqrt{\frac{q_c + q_r - q_s}{R(T_{ave})}}, \quad (3)$$

170 where resistance is determined at the maximum permissible conductor temper-
171 ature from lookup tables. It is common practice to use this equation under
172 conservative assumptions for weather conditions, especially for convective heat
173 loss, to rate transmission lines. This practice, known as the *static line rating*,
174 often leads to stringent limits, not enabling the real-time capacity of the line to
175 be utilized.

176 2.1. Dynamic ratings

177 The steady-state rating given in Eq. 3, is calculated using conservative esti-
178 mates of weather conditions. CIGRE [30] recommends that base ratings should

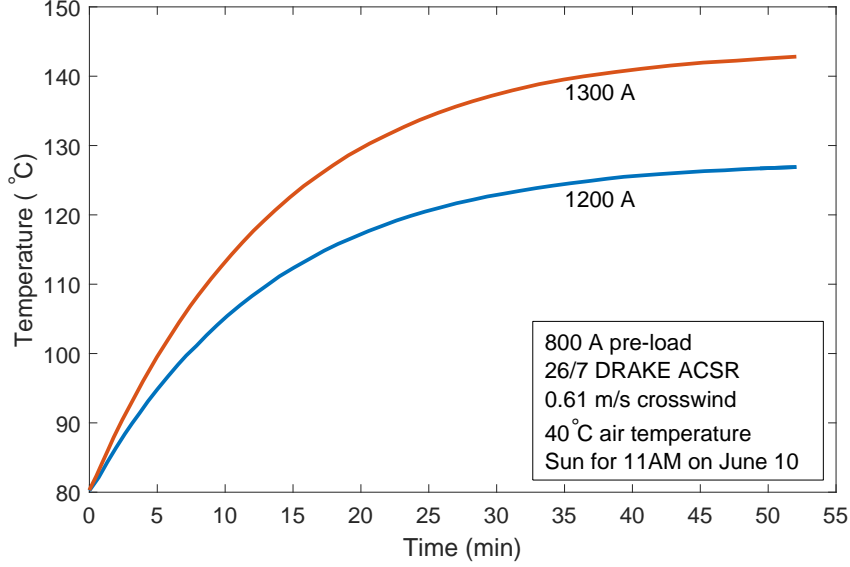


Figure 1: Transient temperature response to a step change in current from 800 to 1200/1300 Amps. Graph adapted from [28].

179 be calculated with an effective wind speed of 0.6 m/s, an air temperature near
 180 the seasonal maximum (40°C summer) and a solar radiation of 1,000 W/m².
 181 In reality the electrical current through the conductor and real-time weather
 182 conditions exposed to the line are constantly changing. In response to these
 183 changes, conductor temperature varies with an associated time scale. Since the
 184 temperature of the conductor is what limits its capacity, we want to track its
 185 temperature in real-time. The change in temperature from an increase in cur-
 186 rent from 800 to 1,200 and 1,300 Amps is shown by the digitized data [28] in
 187 Fig. 1.

188 Transient response of a conductor's temperature to changing current and
 189 weather conditions can be modeled as a first-order ordinary differential equation
 190 (ODE) expressed as

$$191 \quad \frac{dT_{ave}}{dt} = \frac{1}{mC_p} [q_j + q_s - q_c - q_r], \quad (4)$$

192 where mC_p is the total heat capacity of the conductor, given as

$$193 \quad mC_p = \sum m_i C_{pi}, \quad (5)$$

194 where m_i and C_{pi} are the mass per unit length of i^{th} conductor material and the
 195 specific heat of i^{th} conductor material, respectively. Therefore, if the electrical
 196 current and real-time conditions are known, the ODE can be solved numerically
 197 to calculate real-time temperature of the conductor. With the use of a wind
 198 forecasting model, conductor temperature can not only be potentially forecast,
 199 but it can be done at very dense intervals, which may not be feasible with current
 200 hardware solutions. This would give TSPs an unprecedented understanding
 201 of the current and future state of the transmission lines, allowing for better
 202 efficiency of the transmission and generation network.

203 The ODE given in Eq. 4 represents an initial value problem (IVP). The
 204 general form is expressed as

$$205 \quad \frac{dy}{dt} = f(t, y) \quad (6)$$

206 over a time interval

$$207 \quad a \leq t \leq b \quad (7)$$

208 subject to an initial condition

$$209 \quad y(a) = y_0. \quad (8)$$

210 The IEEE Standard 738-2012 does not give a recommended numerical method
 211 to solve the ODE given in Eq. 4. However, it does supply a sample computer
 212 code as a convenience to the user. In that sample code, a first-order accurate
 213 forward Euler method is used. In the standard, it is also pointed out that
 214 other numerical methods may well be more appropriate in certain situations.
 215 Additionally, it is noted that time step size be kept small to reduce numerical
 216 errors.

217 We believe a forward Euler method is too crude for a critical system such
 218 as transmission lines. Therefore we examine the use of a fourth-order accurate
 219 Runge-Kutta (RK4) scheme [31] for improved accuracy and computation time.
 220 The IEEE standard states that there seems to be little advantage in using a
 221 time step greater than one second. This may be true when doing a single
 222 transient temperature calculation for demonstration purposes, as done in the
 223 IEEE standard. However, we are interested in implementing a real-time dynamic

224 rating in practice, which will likely require many thousands of these calculations
 225 to be performed along the length of transmission lines. Therefore, computational
 226 expense may become an issue when using a forward Euler method with small
 227 time steps. An RK4 scheme allow us to assume larger time step sizes while
 228 keeping the error low.

229 An RK scheme can be written as

$$230 \quad y_{i+1} = y_i + \phi(t_i, y_i, h) \cdot h, \quad (9)$$

231 where $\phi(t_i, y_i, h)$ is called the increment function, which is a representative slope
 232 over the interval h . The following 4th order RK scheme (RK4) is used in this
 233 study.

$$234 \quad y_{i+1} = y_i + \frac{1}{6}(k_1 + 2k_2 + 2k_3 + k_4) \cdot h, \quad (10)$$

235 where k 's represent slope estimates.

236 As a test case to compare both numerical methods, we have performed the
 237 same 800 to 1,200 step increase in current provided in the IEEE 738 Standard,
 238 shown in Fig. 1. A normalized L2-norm is used to quantify the difference be-
 239 tween the two methods. The normalized L2-norm is given by

$$240 \quad \|x\| = \frac{1}{N} \sqrt{x_i^2}, \quad (11)$$

241 where N is the number of comparisons between the exact and numerical solution
 242 and x_i is the difference between them. There is no analytical solution, therefore,
 243 a reference value was used as the exact solution. The exact value was calculated
 244 using the RK4 method and a time step of 0.01 seconds.

245 The results are shown in Fig. 2, and tabulated in Table 1. This test case
 246 makes it clear that care needs to be taken with the selection of a numerical
 247 method, the resulting conductor temperature and computation time can be
 248 greatly affected. If a DLR system is put in place it is critically important that
 249 temperature computations can be completed in near real-time while keeping
 250 numerical errors to an acceptable level. Using the RK4 method allows a time
 251 step size of 300s over the Euler of 1s, while keeping numerical errors at the
 252 same order of magnitude. This allows calculations to be completed over 90

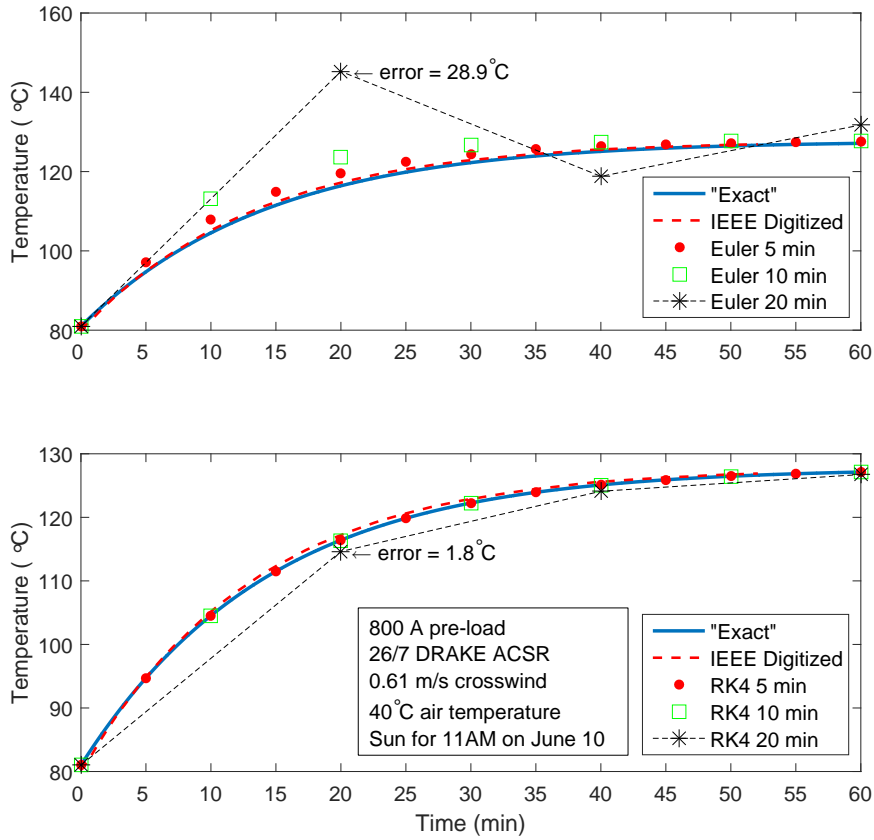


Figure 2: Transient conductor temperature solution using a forward Euler method (top) and a 4th order Runge-Kutta method (bottom) with time steps of 5, 10, and 20 minutes. The “Exact” value was calculated using the RK4 and a time step of 0.01s. IEEE standard solution has been digitized.

253 times faster, potentially reducing computation time from minutes to seconds.
 254 This time could prove critical for TSP, giving them additional time to make
 255 needed transmission decisions. Therefore, we recommend an RK4 scheme for
 256 calculating the temperature of a conductor as it is easy to implement and there
 257 is a clear benefit to it.

258 3. Massively parallel wind solver

259 The need for accurate wind modeling , especially at low speeds and over
 260 complex terrain, were mentioned in recent studies [21, 13]. Steady-state CFD

Table 1: Normalized L2-norm of conductor temperature using a forward Euler and 4th order Runge-Kutta method. The “exact” values are calculated using the RK4 and a time step (dt) of 0.01s. The speedup is based of the Euler calculation with a time step of 1s.

dt(s)	L2-norm		Speedup	
	RK4	Euler	RK4	Euler
1	1.8E-14	1.1E-4	0.3	1
10	9.4E-11	3.4E-3	3.0	10
30	1.3E-8	1.8E-2	9.2	31
60	3.1E-7	5.0E-2	19	61
300	5.1E-4	0.58	93	314
600	1.4E-2	1.8	186	616
1,200	0.52	7.5	367	1,266

261 solutions based on Reynolds-averaged Navier-Stokes (RANS) equations may
 262 not capture the unsteady nature of winds over complex terrain. The large-eddy
 263 simulation technique (LES) is inherently unsteady and generally produces better
 264 results for separated flows over complex terrain. However, LES is expensive in
 265 terms of computational resources, because fine spatial resolutions are needed to
 266 resolve energetic eddies. On the other hand, fine resolutions could be beneficial
 267 to better monitor the conductor temperature along its path. The unsteady
 268 nature of the wind simulations could also help capture the transient response
 269 of the conductor to establish a reliable line rating technique. To this end,
 270 advances in parallel computing technology can help broaden the adoption of
 271 LES technique in practical problems. Graphics processing units offer a relatively
 272 economical solution as a small-footprint computing platform because of their
 273 massively parallel architecture.

274 In this study, we adopt a multi-graphics-processing-unit-accelerated (multi-
 275 GPU), parallel wind solver, GIN3D [32, 33, 34, 35, 36], as an improved solution
 276 for wind modeling over complex terrain. Depending on the mesh size, GIN3D

277 has the potential compute winds over arbitrarily complex terrain faster than
 278 real-time. Computational domain size can range from meters to several kilo-
 279 meters. The computations are accelerated on GPU clusters with a dual-level
 280 parallel implementation that interleaves Message Passing Interface (MPI) with
 281 NVIDIA’s Compute Unified Device Architecture (CUDA). For instance for an
 282 area of approximately 6.5km by 5.7km with a spatial resolution of 15m in the
 283 horizontal and 8m in the vertical, simulations can be 2.2. times faster than
 284 real-time on four Tesla K20 GPUs. In this study, we will execute GIN3D by im-
 285 posing a wind direction inferred from local measurements to assess potential of
 286 a simulation-based DLR approach. Our future goal is to forecast micro-scale at-
 287 mospheric flows over complex terrain with a model-chain approach where lateral
 288 boundary conditions are informed by a mesoscale weather forecasting model.

289 The large-eddy simulation (LES) technique is used in GIN3D for subgrid-
 290 scale turbulence closure. In LES of atmospheric flows, it is common practice to
 291 employ a wall-model due to the complexity and roughness of terrain and the
 292 inadequate resolution in the vicinity of the surface. In particular we pursue a
 293 hybrid Reynolds-averaged Navier-Stokes (RANS) LES technique. We employ
 294 the hybrid eddy viscosity model proposed in [37] which can be written as follows,

$$295 \quad \nu_t = \left[([1 - \exp(-z/h_{RL})] C_S \Delta)^2 + (\exp(-z/h_{RL}) \kappa z)^2 \right] |\bar{S}|, \quad (12)$$

296 where z is the surface-normal distance, h_{RL} is the RANS-LES transition height,
 297 $C_S \Delta$ representing the sub-grid-scale (SGS) mixing length (C_S being the model
 298 coefficient and Δ the LES filter width), and κz representing the RANS mixing
 299 length. The SGS mixing length is determined using the Lagrangian dynamic
 300 SGS methodology [38] applied to the Smagorinsky eddy viscosity model. The
 301 Lagrangian dynamic model is a localized SGS model that does not require any
 302 homogeneous directions in the computational domain. Therefore, it is adequate
 303 for arbitrarily complex terrain. The RANS mixing length is that of Prandtl [39].

304 We prefer a Cartesian method to solve the governing equations as it maps
 305 well to the computer architecture of modern GPUs. The immersed boundary
 306 (IB) method is used to impose boundary conditions on the surface using loga-

307 rithmic reconstructions [40] in conjunction with the above hybrid eddy viscosity
 308 model. Note that the goal is to produce the correct Reynolds stresses at the
 309 surface. Therefore, it is important that the velocity reconstruction scheme is
 310 consistent with eddy viscosity near the surface. A logarithmic reconstruction
 311 therefore is suitable because it is consistent with the Prandtl’s mixing length
 312 model near the surface.

313 While IB methods eliminate cumbersome meshing and poor mesh quality
 314 (e.g. skewed cells), the challenge is to impose the boundary conditions as the
 315 immersed surface will most likely not coincide with the Cartesian grid points.
 316 We employ the direct-forcing approach proposed by [41] and later applied by
 317 [42]. This IB method can be classified as a “sharp interface” IB method, as the
 318 boundary condition at the surface appears explicitly in the method. The first
 319 step of this IB method is to identify the Cartesian grid cells cut by the surface,
 320 which can be challenging with arbitrarily complex terrain. The details of the
 321 geometric pre-processing can be found in [43]. Once the geometric information
 322 is known, the values in near-surface grid cells cut by the immersed surface can
 323 be reconstructed each simulation time step by interpolating between the known
 324 boundary condition at the immersed surface, e.g. the no-slip condition for
 325 velocity, and resolved values from the flow field where the grid cells are not cut
 326 by the immersed surface. The logarithmic reconstruction scheme for velocity
 327 proposed by [40] is revised to explicitly enforce the impermeability condition
 328 over complex terrain. First, the velocity components are projected onto surface-
 329 parallel and surface-normal vectors, $u_{i,t}$ and $u_{i,n}$. The reconstruction scheme for
 330 the normal components is a linear interpolation between the flow at a sufficient
 331 surface-normal distance, z_2 , and the no-slip condition at the immersed surface,

$$332 \quad u_{i,n}|_{z_1} = u_{i,n}|_{z_2} \frac{z_1}{z_2}, \quad (13)$$

333 where z_1 is the IB node wall-normal distance. The impermeability condition
 334 is then explicitly enforced. The tangential reconstruction scheme is based on

Table 2: Simulation parameters. Target domain is centered in the total domain which includes the extension and tapering regions for the periodic boundary conditions.

Domain size (km)			Grid Points			Resolution (m)		
L_x	L_y	L_z	N_x	N_y	N_z	Δx	Δy	Δz
16.0	23.0	1.94	1025	1025	513	29.3	34.2	3.9

335 logarithmic-similarity in the atmospheric surface layer [44] and is given by

$$336 \quad u_{i,t}|_{z_1} = u_{i,t}|_{z_2} \frac{\log(z_1/z_0)}{\log(z_2/z_0)}, \quad (14)$$

337 using the same surface-normal distances as in Eq. 13, where z_0 is the aerody-
 338 namic roughness length.

339 3.1. Simulation setup

340 The target computational domain is $\sim 368\text{km}^2$ shown in Fig. 3. Periodic
 341 boundary conditions were applied in the lateral directions, deemed suitable as
 342 the elevation changes relative to the total height of the computational domain
 343 are small. As complex terrain may not be the same elevation on all sides of the
 344 domain, we extended and tapered the target domain down such that the eleva-
 345 tion is constant along the perimeter of the domain. This added approximately
 346 6-7km to each side. The total domain height is $\sim 2\text{km}$ from the lowest elevation.
 347 The Cartesian grid consisted of ~ 539 million points, giving lateral resolution of
 348 $\sim 30\text{m}$ and vertical resolution of 4m. Simulation parameters are given in Table
 349 3.1.

350 The wind flow is driven by a constant $6.0\text{e-}05\text{m/s}^2$ pressure gradient coming
 351 from the north-east at an angle of 63.3° using meteorological conventions (i.e.
 352 wind coming from north is 0° and clock-wise is positive.). The pressure gradient
 353 was adjusted iteratively to approximately match the observed wind speed at a
 354 weather station over flat terrain. The top of the domain is set to a free-slip
 355 condition. Fluid properties are that of air at standard temperature. Surface
 356 roughness, z_0 , is set to 0.15m, a value suggested in [44] for rural farmland

357 areas. Following [37], the RANS-LES interface, h_{RL} , is set to 31.6m, twice
358 the size of the LES filter width, $\Delta = \sqrt[3]{\Delta x \Delta y \Delta z}$. The flow is initialized by
359 superimposing high-amplitude, low-frequency sinusoidal perturbations onto a
360 rough-surface log-law profile. This was a necessary step as the terrain elevation
361 changes were not enough to trip turbulence unassisted, a further indication that
362 periodic boundary conditions are suitable for this case. The flow was allowed
363 to develop for two hours of simulated time before reaching a stationary state.
364 The wind solver assumes incompressible flow, solving the Poisson equation with
365 geometric multigrid designed for multi-GPUs [34] and uses second-order central
366 difference schemes for spatial derivatives and a second-order Adams-Bashforth
367 scheme for time integration.

368 4. DLR test area

369 Idaho Power Company (IPCo) and Idaho National Laboratory joint test bed
370 area for DLR research is located on the Snake River Plain in southern Idaho.
371 The test site lies in an area of high desert with complex terrain, covering an
372 area approximately 1,500km² with an elevation range of 754m to 1,1198m.

373 Seventeen weather stations were mounted by IPCo/INL team at a height
374 of 10m agl in strategic locations along more than 190km of high-voltage trans-
375 mission lines. Data collection through a cellular network has been underway
376 by IPCo since August of 2010. The measured quantities are wind speed, wind
377 direction, ambient temperature, and solar irradiation. Data from the weather
378 stations is collected every 3 minutes, it is an average of 2s readings over the
379 3-minute time interval. Weather stations use NRG 40C [45] or the APRS
380 #40R [46] three cup anemometers. Both models have similar specifications;
381 wind speed accuracy of 0.1 m/s with a sensor range of 1–96m/s. In Phillips et
382 al. [47] a year-long weather data was analyzed seasonally to demonstrate the
383 limitation of the static rating approach on ampacity.

384 For the simulations used in this paper, we chose a 16km×23km area with an
385 elevation change of over 330m. Figure 3 shows the elevation map and locations

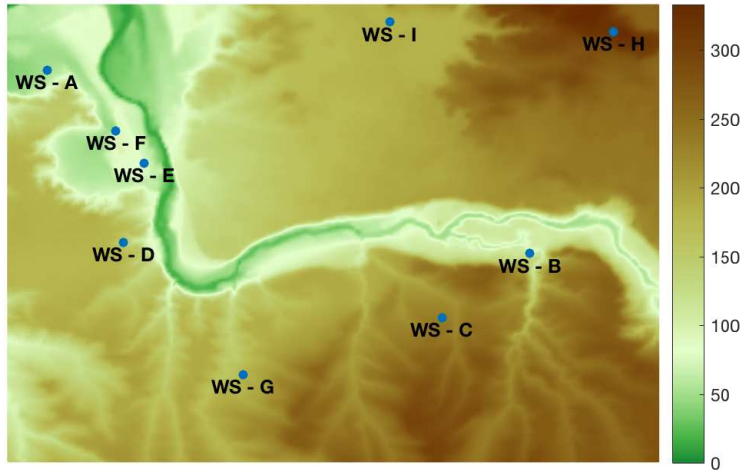


Figure 3: Section of INL/IPCo test site for DLR research, colored by terrain height.

386 of the nine weather stations located in this area.

387 4.1. Test area prevailing winds

388 Wind flow patterns emerge from horizontal surface and atmospheric temper-
 389 ature contrasts on all spatial scales, from global to local size [48]. Both local and
 390 global systems exhibit large regularity of daily and seasonal wind and weather
 391 cycles [49]. This regularity can be largely attributed to the local terrain and
 392 surface properties. Using year-long data starting July 1, 2012 the prevailing
 393 wind direction is illustrated by the wind rose in Fig. 4. Two weather stations
 394 ~ 2 km east of the area investigated were selected because they better repre-
 395 sent the boundary conditions of the simulation, therefore used as discussed in
 396 Section 3.1.

397 Because weather stations operate unattended for a long period and adverse
 398 weather conditions can exist during winter months, it was necessary to validate
 399 the collected data against a common statistical distribution. The distribution
 400 of wind speed is commonly defined using the Weibull probability density func-
 401 tion [50]. During any time interval the two parameter wind speed probability

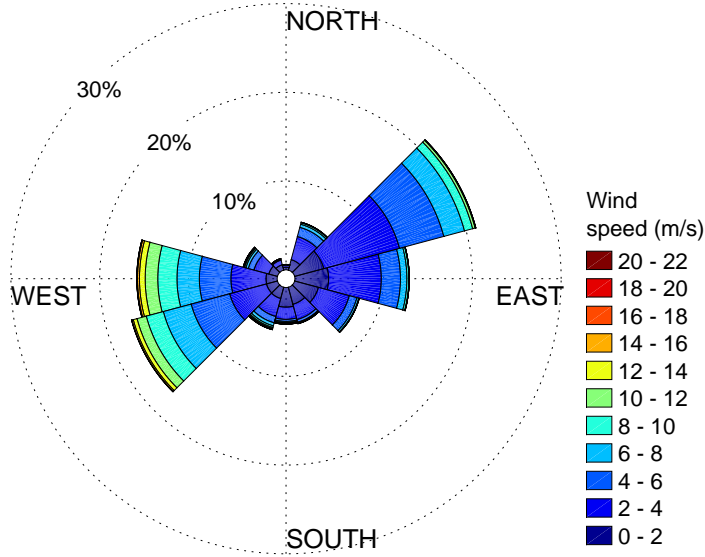


Figure 4: Wind rose of year-long wind data starting July 1, 2012 from two weather ~ 2 km east of the area investigated.

402 is given as

$$403 \quad f(v) = \left(\frac{k}{\lambda}\right) \left(\frac{v}{\lambda}\right)^{k-1} e^{-\left(\frac{v}{\lambda}\right)^k} \quad (15)$$

404 where v is the wind speed, k is the shape parameter, and λ is the scale factor,
 405 which is expected to be close to the mean speed. The Weibull probability density
 406 function of year-long measured wind data at each of the weather stations is
 407 shown in Fig. 5. The nondimensional shape parameter for the collected data
 408 is in agreement with the commonly observed values (i.e. k ranging from 1.6 to
 409 2.4) [50].

410 5. Results

411 To demonstrate the feasibility of a simulation-based DLR approach, we first
 412 compare our wind solver predictions against field data. A horizontal slice of
 413 the eastern region of the target domain in Fig. 3 is the focus of Fig. 6. Eddy
 414 sizes vary visibly over the terrain. Long, streak-like structures with low wind

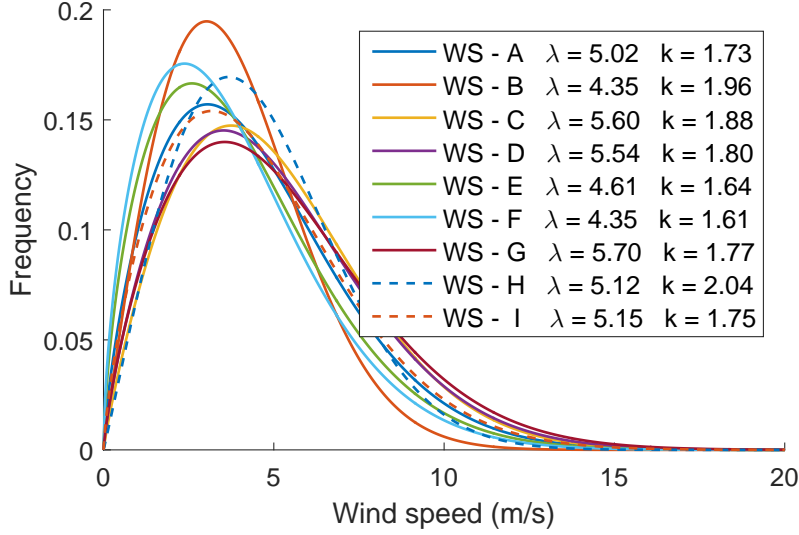


Figure 5: Weibull wind distribution using year-long wind data from each weather station.

415 speed are evident in the vicinity of the surface. The location of the canyon
 416 can be inferred as the flow in to and out of the canyon breaks down the larger
 417 eddies vertically above the canyon into much smaller ones. The wind breaks into
 418 smaller eddies as it blows over the canyons. Additionally, acceleration of the
 419 flow above the canyon can be observed from the color map. We next perform a
 420 statistical evaluation of the wind flow simulation.

421 5.1. Statistical validation of the wind solver

422 To evaluate the wind solver’s performance against anemometer data collected
 423 at select locations across the test bed area, we follow an approach similar to the
 424 one presented in Carvalho et al [23] by using five statistical parameters: the
 425 mean and standard deviation, the root mean squared error (RMSE), the bias,
 426 and the standard deviation of the error (STDE). The mean is given as

$$427 \quad \bar{v} = \frac{1}{N} \sum_{i=1}^N v_i \quad (16)$$

428 where \bar{v} is the mean speed, N is the number of data points, and v_i is the i^{th}
 429 wind speed of either the real-time data or simulation results. The standard

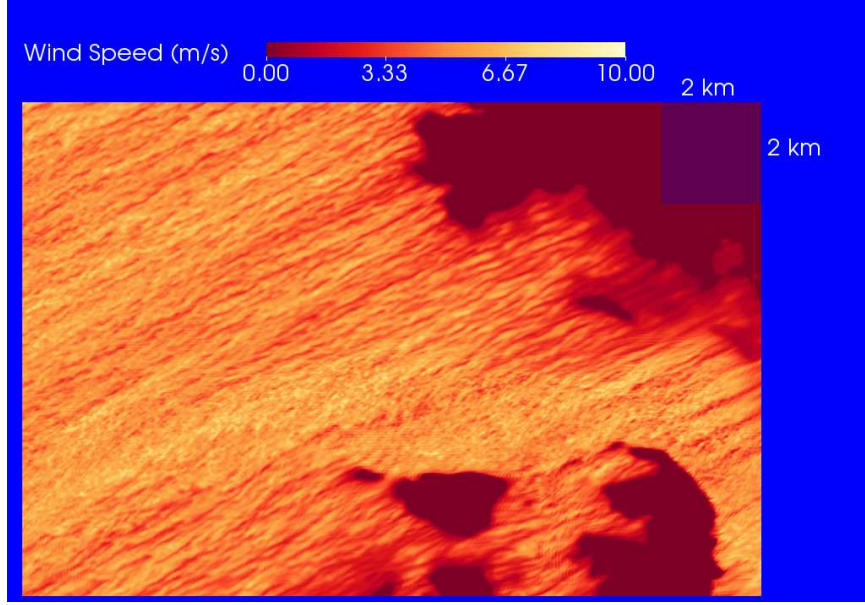


Figure 6: Flow visualization. Horizontal slice across domain focusing on eastern part of the canyon in the target domain. Flow is from upper-right moving to lower-left. 2km \times 2km box provided to show scale.

430 deviation, S_v , is given as

$$431 \quad S_v = \sqrt{\frac{1}{N} \sum_{i=1}^N (v_i - \bar{v})^2} \quad (17)$$

432 and the RMSE is computed as

$$433 \quad RMSE = \left[\frac{1}{N} \sum_{i=1}^N (v'_i)^2 \right]^{1/2} \quad (18)$$

434 where N is the total number of deviations, v' , between the the simulated wind
 435 speed, v^{sim} , and the respective observed wind speed at the weather station,
 436 v^{obs} . The deviation is given as

$$437 \quad v' = v^{obs} - v^{sim} \quad (19)$$

438 The bias is defined as

$$439 \quad Bias = \frac{1}{N} \sum_{i=1}^N v'_i \quad (20)$$

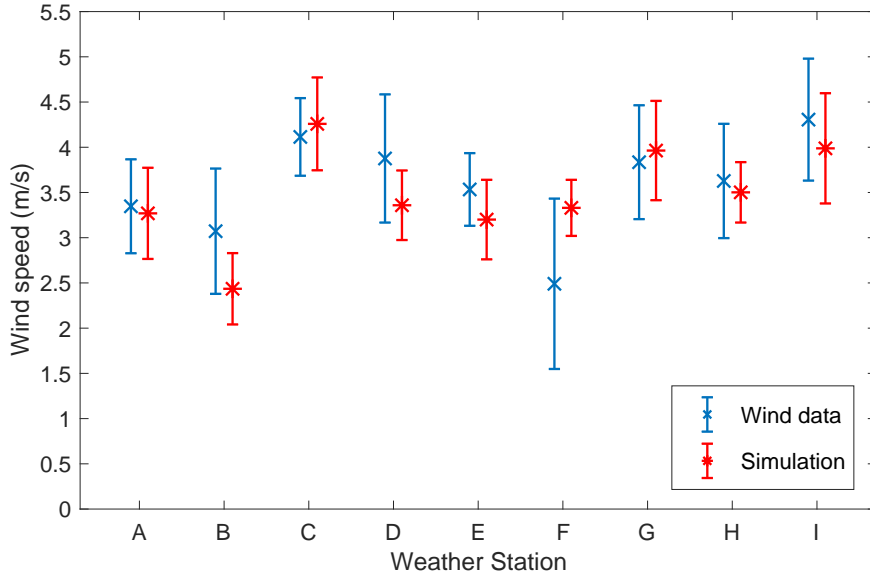


Figure 7: Mean and standard deviation of the field data and simulation results for wind speed

440 and makes possible the evaluation of the data systematic errors. A positive bias
 441 means that the simulations overestimate the measured values.

442 The standard deviation of the error (STDE), helps evaluate the dispersion
 443 of the error and it can be written as

$$444 \quad STDE = [RMSE^2 - Bias^2]^{1/2}. \quad (21)$$

445 The STDE removes from the RMSE possible offsets (biases). A low STDE
 446 shows if a given error is mainly due to a kind of offset that can more easily
 447 be corrected because the underlying physics is correct, whereas a high STDE
 448 represents random error and hints unphysical results.

449 Figure 7 shows that the mean and standard deviation of the wind speed be-
 450 tween the field data and simulation results. We observe that STDE is larger for
 451 weather stations B, D and F than the rest of the weather stations. We attribute
 452 this difference to the challenges of collecting seasonal data from weather stations
 453 that are unattended for long periods. Another issue is that these weather sta-
 454 tions were placed to be close to the powerlines and not necessarily at locations

Table 3: Statistical comparison between the observed field data and simulated results at each weather station. A negative bias represents a simulated wind speed that is greater than the field data readings.

Weather Station	RMSE (m/s)	Bias (m/s)	STDE (m/s)
A	0.684	0.082	0.679
B	1.047	0.634	0.834
C	0.672	-0.141	0.657
D	0.997	0.526	0.847
E	0.680	0.332	0.591
F	1.295	-0.835	0.990
G	0.855	-0.130	0.846
H	0.762	0.124	0.752
I	0.774	0.318	0.706

455 that would capture the dominant wind patterns over the area. It is likely that
 456 these weather stations are picking up local details that may not be represented
 457 in the simulation.

458 The comparison between field and simulation data is further quantified in
 459 Table 3, with an average RMSE value of 0.863, bias of 0.101, and STDE of
 460 0.767. These values are much lower than the values reported in Carvalho et
 461 al. [23]. In Michiorri et al [20] the standard deviation ranged from 0.9 to 1.5,
 462 whereas in our approach, it ranges from 0.6 to 1.0. For these reasons, we judge
 463 our simulation a reasonable realization of the wind conditions for the assumed
 464 global wind direction.

465 5.2. *Dynamic conductor temperature*

466 We perform the transient calculation of the ODE for temperature to demon-
 467 strate the dynamic thermal response of the conductor. Eq. 4, using field data
 468 from June 10, 2013 at weather station B. Wind speed and ambient temperature
 469 values used in the time-marching ODE are updated every three minutes, the

470 rate of field data collection. The initial temperature of the conductor is first
 471 solved using the initial wind speed and steady-state equation in the form

$$472 \quad R(T) = \frac{q_c + q_r - q_s}{I^2} \quad (22)$$

473 After calculating the resistance, the temperature T is extracted from tabulated
 474 data of resistance versus temperature using a linear interpolation. For this hy-
 475 pothetical case we picked ACSR 26/7 as the conductor type. Static rating was
 476 calculated under the summer time assumptions of 0.61m/s wind, full sun on
 477 June 10 at 11AM (30° latitude, 0m elevation), and an ambient temperature of
 478 40°C. Under these assumptions with an allowable maximum conductor temper-
 479 ature of 100°C the ampacity was calculated with Eq. 3, giving 1,025 Amps. We
 480 then imposed a current of 1,025A to the conductor and calculated the dynamic
 481 temperature using the wind speed and ambient temperature field data. Re-
 482 sults, presented in Fig. 8, show that conductor temperature—overall—is much
 483 lower than the assumed static temperature. Equally important, when adverse
 484 conditions persist over long periods of time, TSPs will be informed when con-
 485 ductor temperature is in excess of their limits. Because of these advantages we
 486 recommend using a dynamic calculation method over the static rating practice.

487 As a feasibility test of a simulation-based approach, the conductor tempera-
 488 ture was calculated using both field data and simulation results over a four-hour
 489 period. Since we are investigating the cooling effect of the wind, we kept other
 490 weather conditions constant. The initial conductor temperature used in the
 491 ODE calculation was solved using Eq. 22. We updated the wind speed every
 492 three minutes and solved the dynamic temperature with a RK4 method over
 493 the four hours. Figure 9 shows the true mean estimate and highlights the 99%
 494 confidence interval (CI). Data from nine weather stations are used to quantify
 495 the uncertainty or CI. The true mean estimate, v' is given as

$$496 \quad v' = \bar{v} \pm CI (\%P) \quad (23)$$

497 where CI is the confidence interval at a given probability, P , and is defined as

$$498 \quad CI = t_{df,P} \cdot S_{\bar{v}} \quad (24)$$

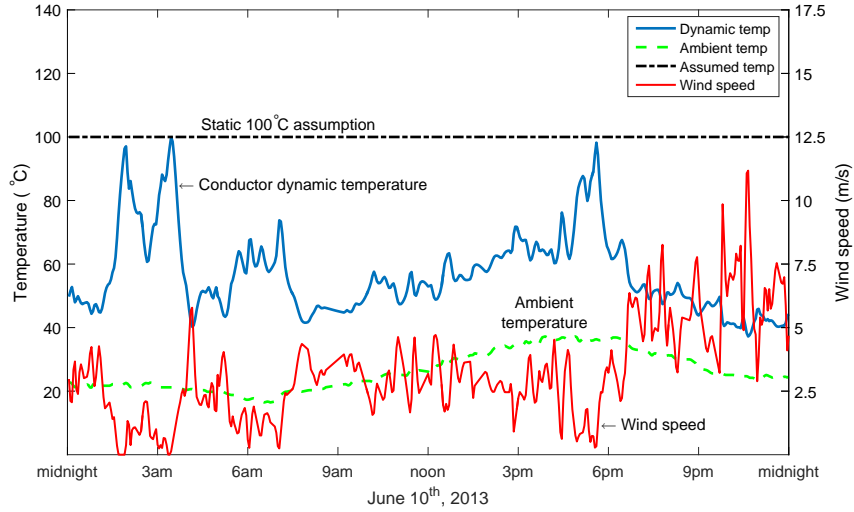


Figure 8: Conductor dynamic temperature calculated using wind speed and temperature from field data and compared with the assumed 100 °C static temperature when loaded with 1,025 Amps.

499 here $t_{df,P}$ is the statistical t-value with degrees of freedom, df . The degrees of
 500 freedom is the number of data points minus one. The standard error, $S_{\bar{v}}$, is
 501 defined as

$$502 \quad S_{\bar{v}} = \frac{S_v}{\sqrt{N}} \quad (25)$$

503 where S_v is the standard deviation and N is the number of data points.

504 There are two important conclusions to take away from Fig. 9. First, the
 505 conductor temperature is much lower than the 100°C imposed by the static
 506 rating. Second, conductor temperature variation relative to its location is sig-
 507 nificant as evidenced by the confidence interval. Spatial variation of conductor's
 508 temperature justifies the need to resolve wind field along the length of the line
 509 to identify critical segments.

510 5.3. Dynamic ampacity

511 When the conductor is below its maximum allowable temperature, any
 512 amount of current can be put on the conductor for a limited amount of time.

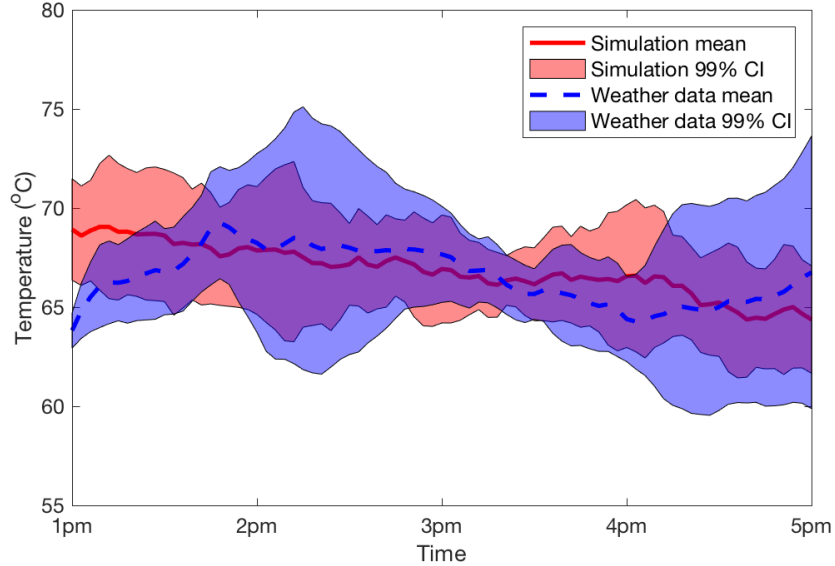


Figure 9: Resulting conductor temperature using the field data and simulation results. The highlighted area represents the 99% confidence interval.

513 We therefore calculate the dynamic ampacity using the conductors present tem-
 514 perature and use an iterative method to solve the current that will heat the
 515 conductor to 100°C in 15 minutes. To demonstrate this, we show a hypotheti-
 516 cal case using ACSR 27/6 conductor with an initial temperature of 60°C , wind
 517 speed of 3.5m/s , 40°C ambient temperature, and full sun. The ampacity is cal-
 518 culated to be $1,616\text{A}$ and the heating can be seen in Fig. 10. If the steady-state
 519 thermal rating, Eq. 3, is used under these conditions the ampacity would be at
 520 $1,571\text{A}$ and the conductor response would have to be assumed instantaneous. In
 521 other words a dynamic ampacity calculation method would enable the operator
 522 to see the actual thermal response of the conductor and its ability to ride out
 523 sudden drops in wind speed as it takes some time for the conductor to heat up.

524 The dynamic ampacity across the test area is therefore calculated using the
 525 temperature calculated in section 5.2 and the 15 minute transient temperature
 526 response to reach 100°C . The resulting ampacity mean and 99% CI using both
 527 field data and simulation results are shown in Fig. 11. The results show that
 528 there is significant additional capacity available that is not being utilized.

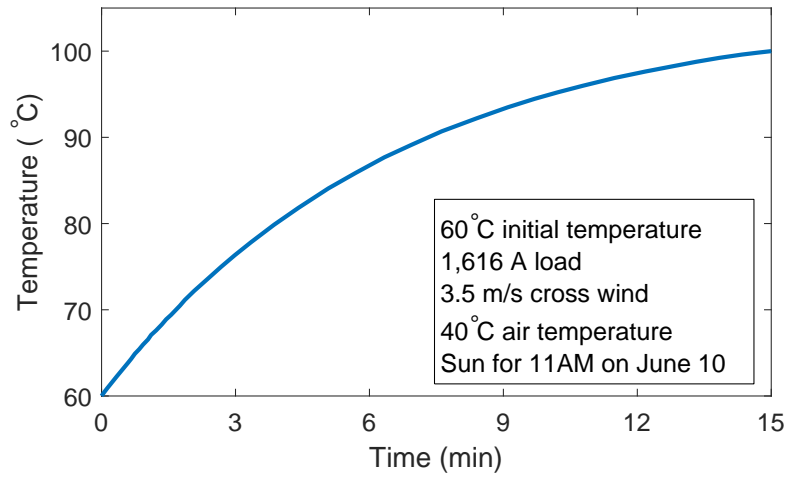


Figure 10: Conductor heating from 60 to 100°C in 15 minutes with a current of 1,616 Amps.

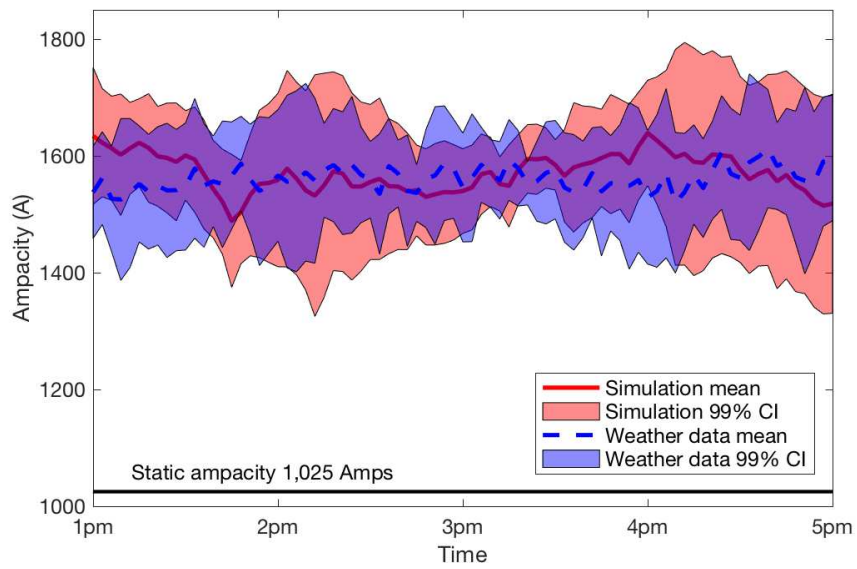


Figure 11: Resulting dynamic ampacity using field data and simulation results, i.e. this ampacity will heat the conductor from its present temperature to 100°C in 15 minutes. The highlighted area represents the 99% confidence interval.

529 **6. Conclusions**

530 Dynamic line rating (DLR) holds great promise to alleviate transmission
531 congestion that may hinder integration of new power generation. Using actual
532 weather data from measurements and an LES-based micro-scale wind solver, we
533 demonstrated that ampacity of transmission lines in windy areas with complex
534 terrain can be increased by 40-50% through the DLR concept. Our simulation-
535 based approach is non-intrusive for the powerlines, and it is potentially much-
536 more economical than building new transmission lines.

537 The use of a multi-GPU accelerated solver was critical to the success of our
538 study. Instead of using a commercially available general-purpose computational
539 fluid dynamics solver, we carefully selected our numerical methods and param-
540 eterizations to develop a fast wind solver, which was a multi-year effort with
541 multiple developers [32, 33, 34, 35, 36]. The hardware-oriented design of our
542 numerical solver —combined with the superior computing power of GPUs—
543 enabled us to accommodate spatial and temporal resolutions that are much
544 finer than the current practice for complex terrain wind simulations. Adop-
545 tion of fine spatial resolutions is important for the resolution of terrain-induced
546 motions, leading to more accurate line ratings. A potential benefit of using a
547 multi-GPU accelerated solver is that simulations can be performed on worksta-
548 tions or clusters that have a much smaller footprint than central processing unit
549 (CPU) based computing platforms.

550 Statistical analysis of simulation data for wind speed showed a very good
551 agreement with field data. Additionally, we demonstrated that a transient cal-
552 culation of the conductor temperature offers many advantages over the current
553 practice based on the steady-state response of a conductor. A transient calcula-
554 tion enables us to take advantage of the thermal capacity of a conductor under
555 variable wind conditions when considering a dynamic rating approach. We
556 found that a fourth-order Runge-Kutta scheme performs much better in terms
557 of accuracy and computation time than the forward Euler method suggested in
558 the IEEE-738-2012 standard.

559 **ACKNOWLEDGMENTS**

560 This material is based upon work supported by the National Science Foun-
561 dation under Grant No. 1056110 and 1229709. The second author would like to
562 acknowledge the University of Idaho President’s Doctoral Scholars Award. We
563 extend our thanks to Idaho Power for sharing the raw wind data, and helpful
564 discussions with Kurt Meyers and Jake Gentle of Idaho National Laboratory on
565 dynamic line rating concept.

566 **References**

- 567 [1] Wind vision: A new era for wind power in the United States, Tech. rep.,
568 U.S. Department of Energy (2015).
- 569 [2] D. of Energy, 20% Wind Energy by 2030: Increasing Wind Energy’s Contri-
570 bution to U.S. Electricity Supply, Technical report DOE/GO-102008-2567,
571 2008.
- 572 [3] A. Arroyo, P. Castro, R. Martinez, M. Manana, A. Madrazo, R. Lecuna,
573 A. Gonzalez, Comparison between IEEE and CIGRE thermal behaviour
574 standards and measured temperature on a 132-kv overhead power line,
575 MDPI Energies 8 (2015) 13660–13671.
- 576 [4] J. Metevosyan, Wind power in areas with limited transmission capacity, in:
577 T. Ackermann (Ed.), Wind power in power systems, John Wiley and Sons,
578 2005, Ch. 20, pp. 433–501.
- 579 [5] R. S. Jorge, E. G. Hertwich, Environmental evaluation of power transmis-
580 sion in norway, Elsevier: Applied Energy 101 (2013) 513–520.
- 581 [6] J. Hall, A. Deb, Prediction of overhead transmission line ampacity by
582 stochastic and deterministic models, IEEE: Power Delivery 3 (2) (1988)
583 789–800.

- 584 [7] J. Reding, A method for determining probability based allowable current
585 ratings for BPA's transmission lines, *IEEE: Power Delivery* 9 (1) (1994)
586 153–161.
- 587 [8] P. Pytlak, P. Musilek, E. Lozowski, J. Toth, Modelling precipitation cooling
588 of overhead conductors, *Elsevier: Electric Power Systems Research* 81 (12)
589 (2011) 2147–2154.
- 590 [9] J. Cho, J. Kim, J. Lee, J. Kim, I. Song, J. Choi, Development and im-
591 provement of an intelligent cable monitoring system for underground dis-
592 tribution networks using distributed temperature sensing, *MDPI: Energies*
593 7 (2) (2014) 1076–1094.
- 594 [10] C. Holyk, H. D. Liess, S. Grondel, H. Kanbach, F. Loos, Simulation and
595 measurement of the steady-state temperature in multi-core cables, *Elsevier:*
596 *Electric Power Systems Research* 116 (2014) 54–66.
- 597 [11] J. Hosek, Dynamic thermal rating of power transmission lines and renew-
598 able resources, in: *ES1002 Workshop*, Paris, France, 2011, pp. 1–3.
- 599 [12] J. Heckenbergerova, J. Hosek, Dynamic thermal rating of power transmis-
600 sion lines related to wind energy integration, in: *Environment and Elec-*
601 *trical Engineering (EEEIC)*, 2012 11th International Conference on, 2012,
602 pp. 798–801.
- 603 [13] E. Fernandez, I. Albizu, M. Bedialauneta, A. Mazon, P. Leite, Review of
604 dynamic line rating systems for wind power integration, *Renewable and*
605 *Sustainable Energy Reviews* 53 (2016) 80 – 92.
- 606 [14] S. Uski-Joutsenvuo, R. Pasonen, S. Rissanen, Maximising power line trans-
607 mission capability by employing dynamic line ratings: Technical survey and
608 applicability in Finland, *Research report*, VTT-R-01604-13, 2013.
- 609 [15] EPRI, *Increased Power Flow Guidebook: Increasing Power Flow in Trans-*
610 *mission and Substation Circuits*, Palo Alto, CA. 1010627 (2005).

- 611 [16] T. O. Seppa, A practical approach for increasing the thermal capabilities
612 of transmission lines, *IEEE Transactions on Power Delivery* 8 (3) (1993)
613 1536–1550.
- 614 [17] T. O. Seppa, R. D. Mohr, J. Stovall, Error sources of real-time ratings
615 based on conductor temperature measurements, Report to CIGRE WG
616 B2.36 (2010) 20–21.
- 617 [18] J. Gentle, K. S. Myers, T. Baldwin, I. West, K. Hart, B. Savage, M. Ellis,
618 P. Anderson, Concurrent wind cooling in power transmission lines, in: 2012
619 Western Energy Policy Research Conference, 2012. INL/CON-12-27012.
- 620 [19] D. M. Greenwood, J. P. Gentle, K. S. Myers, P. J. Davison, I. J. West,
621 J. W. Bush, G. L. Ingram, M. C. Troffaes, A comparison of real time
622 thermal rating systems in the U.S. and the U.K., *IEEE Transactions on*
623 *Power and Delivery* 29 (4).
- 624 [20] A. Michiorri, P. C. Taylor, S. C. E. Jupe, Overhead line real-time rating
625 estimation algorithm: Description and validation, *Proceedings of the In-*
626 *stitution of Mechanical Engineers, Part A: Journal of Power and Energy*
627 224 (3) (2010) 293–304.
- 628 [21] A. Michiorri, H.-M. Nguyen, S. Alessandrini, J. B. Bremnes, S. Dierer,
629 E. Ferrero, B.-E. Nygaard, P. Pinson, N. Thomaidis, S. Uski, Forecasting
630 for dynamic line rating, *Renewable and Sustainable Energy Reviews* 52
631 (2015) 1713 – 1730.
- 632 [22] M. G.-G. David Carvalho, Alfred Rocha, C. Santos, WRF wind simula-
633 tion and wind energy production estimates forced by different reanalyses:
634 Comparison with observed data for Portugal, *Applied Energy* 117 (2014)
635 116–126.
- 636 [23] M. G. David Carvalho, Alfred Rocha, C. Santos, A sensitivity study of the
637 wrf model in wind simulation for an area of high wind energy, Elsevier:
638 *Environmental Modelling & Software* 33 (2012) 23–34.

- 639 [24] M. Bhaskar, A. Jain, N. V. Srinath, Wind speed forecasting: Present status,
640 Power System Technology (POWERCON), 2010 International Conference
641 (2010) 1–6.
- 642 [25] M. Negnevitsky, P. Mandal, A. Srivastava, An overview of forecasting prob-
643 lems and techniques in power systems, Power Energy Society General Meet-
644 ing, 2009. PES 2009. IEEE (2009) 1–4.
- 645 [26] S. Soman, H. Zareipour, O. Malik, P. Mandal, A review of wind power
646 and wind speed forecasting methods with different time horizons, North
647 American Power Symposium (NAPS) (2010) 1–8.
- 648 [27] B. Banerjee, D. Jayaweera, S. Islam, Risk constrained short-term schedul-
649 ing with dynamic line ratings for increased penetration of wind power,
650 Renewable Energy 83 (2015) 1139 – 1146.
- 651 [28] IEEE, IEEE standard 738-2012: IEEE standard for calculating the current-
652 temperature relationship of bare overhead conductors.
- 653 [29] CIGRE, The thermal behaviour of overhead conductors, *CIGRE WG 12*.
- 654 [30] CIGRE Working Group B2.12, Guide for selection of weather parameters
655 for bare overhead conductor ratings, Tech. Rep. 299 (August 2006).
- 656 [31] S. C. Chapra, R. P. Canale, Numerical Methods for Engineers, 6th Edition,
657 McGraw Hill, Boston, MA, 2010.
- 658 [32] J. C. Thibault, I. Senocak, Accelerating incompressible flow computa-
659 tions with a Pthreads-CUDA implementation on small-footprint multi-
660 GPU platforms, *Journal of Supercomputing* 59 (2) (2012) 693–719.
- 661 [33] D. A. Jacobsen, I. Senocak, Multi-level parallelism for incompressible flow
662 computations on GPU clusters, *Parallel Computing* 39 (1) (2013) 1 – 20.
663 doi:<http://dx.doi.org/10.1016/j.parco.2012.10.002>.

- 664 [34] D. A. Jacobsen, I. Senocak, A full-depth amalgamated parallel 3D geomet-
665 ric multigrid solver for GPU clusters, in: 49th AIAA Aerospace Science
666 Meeting, no. AIAA-2011-946, Orlando, FL, 2011.
- 667 [35] R. DeLeon, K. Felzien, I. Senocak, Toward a GPU-accelerated immersed
668 boundary method for wind forecasting over complex terrain, in: Proceed-
669 ings of the ASME 2012 Fluids Engineering Division Summer Meeting, no.
670 FEDSM2012-72145, 2012.
- 671 [36] R. DeLeon, D. Jacobsen, I. Senocak, Large-eddy simulations of turbulent
672 incompressible flows on GPU clusters, *Computing in Science and Engineer-*
673 *ing* 15 (1) (2013) 26–33.
- 674 [37] I. Senocak, A. Ackerman, M. Kirkpatrick, D. Stevens, N. Mansour, Study
675 of near-surface models for large-eddy simulations of a neutrally stratified
676 atmospheric boundary layer, *Boundary-Layer Meteorology* 124 (2007) 405–
677 424.
- 678 [38] C. Meneveau, T. Lund, W. Cabot, A lagrangian dynamic subgrid-scale
679 model of turbulence, *Journal of Fluid Mechanics* 319 (1996) 353–385.
- 680 [39] L. Prandtl, Bericht über die Entstehung der Turbulenz, *X. Angew. Math.*
681 *Mech.* 5 (1925) 136 – 139.
- 682 [40] I. Senocak, A. Ackerman, D. Stevens, N. Mansour, Topography modeling
683 in atmospheric flows using the immersed boundary method, in: *Annual*
684 *Research Briefs*, Center for Turbulence Research, NASA-Ames/Stanford
685 Univ., Palo Alto, CA, 2004, pp. 331–341.
- 686 [41] J. Mohd-Yusof, Combined immersed boundary/B-spline methods for sim-
687 ulations of flow in complex geometries, *Annual Research Briefs*, Center for
688 Turbulence Research, NASA-Ames/Stanford University (1997).
- 689 [42] R. Verzicco, J. Mohd-Yusof, P. Orlandi, D. Haworth, Large eddy simulation
690 in complex geometric configurations using boundary body forces, *AIAA*
691 *Journal* 38 (2000) 427–433.

- 692 [43] I. Senocak, M. Sandusky, R. DeLeon, D. Wade, K. Felzien, M. Budnikova,
693 An immersed boundary geometric preprocessor for arbitrarily complex ter-
694 rain and geometry, *J. Atmos. Ocean. Tech.* 32 (11) (2015) 2075–2087.
- 695 [44] R. B. Stull, *An Introduction to Boundary Layer Meteorology*, Kluwer Aca-
696 demic Publishers, Dordrecht, Netherlands, 1988.
- 697 [45] Renewable NRG Systems, Hinesburg, Vermont, NRG 40C Anemometer
698 (March 2015).
- 699 [46] APRS World, LLC, Winona, MN, APRS #40R (2015).
- 700 [47] T. Phillips, I. Senocak, J. Gentle, K. Myers, P. Anderson, Investigation of
701 a dynamic power line rating concept for improved wind energy integration
702 over complex terrain, in: *Proceedings of the ASME 2014 4th Joint US-*
703 *European Fluids Engineering Division Summer Meeting*, no. FEDSM2014-
704 21377, 2014.
- 705 [48] S. Emeis, *Wind Energy Meteorology: Atmospheric Physics for Wind Power*
706 *Generation*, Springer, Verlag Berlin Heidelberg, 2013.
- 707 [49] A. K. Deb, *Powerline Ampacity System; Theory, Modeling, and Applica-*
708 *tions*, CRC Press, Boca Raton London New York Washington, D.C., 2000.
- 709 [50] M. Brower (Ed.), *Wind resource assessment: a practical guide to developing*
710 *a wind project*, John Wiley & Sons, Hoboken, NJ, 2012.